# Growth of $MoS_2$ nanosheets on M@N-doped carbon particles (M= Co, Fe or CoFe Alloy) as an efficient electrocatalyst toward hydrogen evolution reaction

Sayyar Ali Shah,[1] Li Xu,[1] Rani Sayyar,[1] Ting Bian,[1] Zeyu Liu,[1] AihuaYuan,[1,*] Xiaoping Shen,[2] Iltaf Khan,[4] Asif Ali Tahir,[3] Habib Ullah[3,*]

[1]School of Environmental & Chemical Engineering Jiangsu University of Science and Technology Zhenjiang 212003, P. R. China

[2]School of Chemistry and Chemical Engineering Jiangsu University Zhenjiang 212013, P. R. China

[3]Environment and Sustainability Institute, University of Exeter, Penryn Campus, Penryn, Cornwall TR10 9FE, United Kingdom

[4]Key Laboratory of Functional Inorganic Material Chemistry, School of Chemistry and Materials Science, Heilongjiang University Harbin 150080, P. R. China

## Abstract

The design and synthesis of a highly active noble metal-free electrocatalyst for hydrogen evolution reaction (HER) from water splitting are crucial for renewable energy technologies. Herein, we report the growth of molybdenum disulfide ($MoS_2$) on N-doped carbon encapsulated metal particles (M@NDC@$MoS_2$, where M= Co, Fe or CoFe alloy) as a highly active electrocatalyst for HER. The hierarchical $MoS_2$ nanosheets are grown on M@NDC using the hydrothermal method. Our results show that CoFe@NDC@$MoS_2$ hybrid spheres exhibit excellent HER performance with an overpotential of 64 mV at a current density of 10 mA $cm^{-2}$ and a small Tafel slope of 45 mV $dec^{-1}$. In addition, CoFe@NDC@$MoS_2$ hybrid spheres have good long-term stability and durability in acidic conditions. Besides, density functional theory (DFT) simulations of the

proposed catalysts are performed and suggest that the superior catalytic activity of CoFe@NDC@$MoS_2$ is due to the optimal electron transfer from CoFe@NDC nanoparticles to $MoS_2$ nanosheets. This electron transfer facilitates $H^+$ interaction and adsorption, leading to a decreased Gibbs free energy ($\Delta G_{H^*} \approx 0.08$ eV) and local work function on the surface, which consequently enhances the HER performance.

**Keywords:** Electrocatalyst, Hydrogen evolution reaction, Molybdenum disulfide, N-doped carbon encapsulated metal particles, Density functional theory

## 1. Introduction

To avoid energy crises and environmental issues, the development of clean and sustainable energy sources is crucial.[1-3] Hydrogen is one of the preferable clean and sustainable energy sources especially produce from water splitting.[1-4] Generally, highly reactive electrocatalytic materials are required for HER during water splitting. Platinum-based materials (PBM) are efficient electrocatalysts for HER,[1-3] however, scarcity and high cost limit their large-scale hydrogen production. In order to avoid this dependency on expensive precious PBM catalysts, it is necessary to develop high-performing yet low-cost catalysts. This precious PBM can be replaced by fabricating and designing cheap and earth metal materials with highly electrocatalytic activity for HER. In these regards, some competitive transition metal-based sulfides, selenide, nitrides, phosphides, carbide, and oxides materials have been synthesized and designed as good electrocatalysts for HER.[5-11]

Over the past few years, Molybdenum disulfide ($MoS_2$) nanosheets are emerged as a good candidate for electrocatalytic HER due to low cost, rich active site on the edges, and good stability in acidic media.[12-14] Both theoretical calculations and experimental results reveal that the active site of $MoS_2$ nanosheets is along the exposed edges.[12-16] However, the exposed active site at

the edges of $MoS_2$ nanosheets greatly decreases by the inherent stacking among $MoS_2$ layers due to van der Waals forces. The synthesis and designing of $MoS_2$ nanosheets with highly exposed edges are a very promising approach to enhance its electrocatalytic HER performance. So far, many efforts have been devoted to fabricating $MoS_2$ nanosheets with highly exposed edges.[15-17] Additionally, the HER performance of $MoS_2$ nanosheets can be further improved by other strategies, such as hetero-atoms doping, interface engineering, disorder engineering, increased defects, expanded interlayer spacing, and basal plane activation.[18-23] Despite these approaches, the HER performance of $MoS_2$ is still poor compared to that of PBM.

The growth of semiconductor $MoS_2$ nanosheets on conducting substrate can further enhance the HER performance. Basically, the semiconducting nature of $MoS_2$ nanosheets restricts the electron transfer rate in the catalytic process and consequently reduces the HER performance. On the other hand, carbonaceous materials such as graphene, carbon nanotubes, glassy carbon, carbon paper, and carbon cloth, can be used as growing substrates and conducting cannel for $MoS_2$.[24-27] Recently, $MoS_2$ nanosheets grown carbon encapsulated materials were reported for Li-ions batteries applications.[28-30] Wang et al. reported the growth of $MoS_2$ on N-doped carbon-coated $TiO_2$ nanotube ($TiO_2$@NC@$MoS_2$) with hierarchical nanotubes morphology for enhanced lithium storage, using a step-by-step method.[28] Zhang group reported Si@C@$MoS_2$ composites for lithium-ion batteries by molten salt magnesiothermic reduction, resorcinol formaldehyde coating, and hydrothermal process.[29] However, the intrinsic conductivity of carbonaceous materials becomes lower with oxygen functionalization and growth or deposition of other semiconductor materials on them. To overcome this issue, metallic particles encapsulated in carbonaceous materials can maintain the high conductivity of the material and accelerate the electron transfer rate to $MoS_2$ nanosheets. Recently, evidence of electron transformation from the metallic particle

to the surface of carbon is reported.[31-33] A comprehensive analysis of the reported work led us to conclude that it is vital to grow $MoS_2$ on carbon encapsulated metal nanoparticles as an HER electrocatalyst for outstanding performance.

Here, we report the growth of $MoS_2$ nanosheets on N-doped carbon encapsulated metal nanoparticles for electrochemical HER performance, using hydrothermal method. It is found that $MoS_2$ vertically grows on M@NDC and exposes maximum edges for HER catalytic activity. The as-prepared CoFe@NDC@$MoS_2$ hierarchical sphere displays outstanding HER performance with an overpotential of 64 mV at a current density of 10 mA $cm^{-2}$ and a small Tafel slope of 45 mV $dec^{-1}$. Besides, CoFe@NDC@$MoS_2$ hierarchical sphere exhibits good long-term stability in acidic conditions. Moreover, DFT calculations are performed to get insights into the enhanced HER performance of CoFe@NDC@$MoS_2$ electrocatalyst, which confirm and validate our experimental data.

## 2. Experimental section

### 2.1 Synthesis of M@NDC particles

CoFe@NDC particles were synthesized through pyrolysis. Typically, equal amount (0.3 g) of each $K_3[Fe(CN)_6]_3$, $Fe(CH_3CO_2)_2$, $K_3[Co(CN)_6]_3$ and $Co(CH_3CO_2)_2 \cdot 4H_2O$ precursor and 0.1 g of urea were grounded together to obtain a solid powder and then dispersed in ethanol/water mixture. After evaporation of the solvent, the precursor mixtures were transferred to quartz tube and pyrolyzed tube furnace at 700 ºC for 2 h under the nitrogen atmosphere. When the furnace was cooled to room temperature, the product was collected and washed with water and ethanol. Then the product was dispersed in 1M $H_2SO_4$ solution for 1h under very slow stirring. The product was washed again with water and ethanol and kept at 50 ºC in a vacuum oven for drying.

The Co@NDC and Fe@NDC particles were prepared with similar procedures and conditions. The 0.3 g of $K_3[Co(CN)_6]_3$ and $Co(CH_3CO_2)_2 \cdot 4H_2O$ precursor and 0.1 g urea were used for the synthesis of Co@NDC particles, while 0.3 g of $K_3[Fe(CN)_6]_3$ and $Fe(CH_3CO_2)_2$ precursor and 0.1 g urea were used for the synthesis of Co@NDC particles.

### 2.2 Synthesis of ethylenediamine trimolybdate $Mo_3O_{10}(C_2H_{10}N_2)$ wires

Ethylenediamine trimolybdate wires were synthesized according to the reported method of Gao *et. al*.[34] Briefly, $(NH_4)_6Mo_7O_{24} \cdot 4H_2O$ (0.1 g) was dispersed in water under stirring. Then ethylenediamine (0.85 mL) was added to it. The HCl (0.5 M) solution was dropwise poured into the mixture until the pH value reached 4.5. Then, the reaction mixture was kept in an oil bath at 50 °C for 2 h with constant stirring. The product was collected, washed, and dried in a vacuum oven at 50 °C for 20 h.

### 2.3 Synthesis of M@NDC@$MoS_2$ hybrids.

The $MoS_2$ nanosheets were grown on M@NDC particles by hydrothermal method. 0.28 g of L-cysteine was dissolved in water to form an aqueous solution. Then M@NDC (0.35 g) and $Mo_3O_{10}(C_2H_{10}N_2)$ wires (0.35 g) were added in 15 mL aqueous solution of L-cysteine under magnetic stirring at room temperature. The mixture was poured into a Teflon-lined stainless-steel autoclave (25 mL) and heated at 200 ºC for 16 h. The product was collected by centrifugation and washed with distilled water/ethanol mixture. The final product is obtained after drying in the vacuum oven for 20 h.

### 2.4 Synthesis of NDC@$MoS_2$-A sphere and NDC-A

The CoFe@NDC@$MoS_2$ and CoFe@NDC samples were treated with 1M $H_2SO_4$ solution for 30 h to obtain NDC@$MoS_2$-A sphere and NDC-A (where A represent the sample treated with acid).

## 2.5 Characterizations

The morphologies and micros-structures of products were observed by scanning electron microscope (SEM Hitachi S-4800) and transmission electron microscope (TEM, JEM-2010), respectively. The chemical composition of the as-prepared samples was investigated by energy-dispersive X-ray (EDX) spectroscopes equipped with SEM and TEM. The X-ray diffractometer (XRD, Bruker D-8 Advanced diffractometer) with Cu Kα radiation source (λ = 1.5406 Å) was applied to study the crystal phase composition of the as-prepared samples. Raman spectra of representative samples were acquired on a Raman spectrometer (a JYHR800) using a 532 nm laser source. The X-ray photoelectron spectroscopy (XPS) was performed to study the composition and valence state of elements of a representative sample on a Thermo ESCALAB 250XI system with Al Kα X-ray as an excitation source.

## 1.6 Electrochemical tests for HER

The electrochemical measurements were carried out in a three-electrode (stagnant cell) system on an electrochemical workstation (CHI 760D, Shanghai, Chen hua Co. LTD). The working electrode was a Glassy carbon electrode. The counter electrode was a carbon rod while the saturated calomel electrode (SCE) is used as a reference electrode. The prepared catalyst (4 mg) and 5 wt% Nafion solution (30 μL) were sonicated in 1 mL of absolute ethanol for 30 min to obtain a homogeneous ink. To perform HER electrocatalytic activity, 5 μL of ink was loaded onto a working electrode, and Cyclic voltammograms (CVs) were scanned between 0 and -0.6 V *vs* SCE in 0.5 M $H_2SO_4$ solution at a scan rate of 100 $mVs^{-1}$ for 40 cycles. Then, the linear sweep voltammetry (LSV) with a scan rate of 5 $mVs^{-1}$ was conducted in the same acidic solution. The potentials were converted to reversible hydrogen electrodes (RHE). The stability test of CoFe@NDC@$MoS_2$ sample was estimated by measuring 2000 CV cycles at a scan rate of 100 $mVs^{-1}$ from 0 to -0.5 V vs. SCE in

the same solution. After 2000 cycles, the LSV was measured. To calculate the electrochemical active surface area of the product, CV was tested by measuring double-layer capacitance ($C_{dl}$) under the potential window of 0~0.1 V vs. SCE with various scan rates such as 10, 20, 30, 40, and 50 mV $s^{-1}$. Electrochemical impedance spectroscopy (EIS) was performed at a frequency range of 100 kHz to 100 mHz with an AC voltage of 5 mV in 0.5 $H_2SO_4$ solution. In this work, we used 0.5 M $H_2SO_4$, $E_{RHE} = E_{SCE} + 0.2458$ V.

### 2.7 Computational methods

Density functional theory (DFT) calculations of the experimentally observed electrocatalysts were performed on Quantum ATK[35] and the visualizations are achieved on VESTA and vnl Version 2019.12.[36] In order to model the experimentally observed $MoS_2$ nanosheets, grown on nitrogen-doped carbon encapsulated metals nanoparticles, (i) a C shell, a single shell of carbon 60 is doped with 5% nitrogen (NDC), nitrogen-doped carbon encapsulated CoFe nanoparticles (CoFe@NDC), and single-layer $MoS_2$ nanosheets, (ii) Then Fe@NDC, Co@NDC, and CoFe@NDC particles have interacted with a single layer of $MoS_2$ (Fig. S1). The origin of HER activity of M@NDC@$MoS_2$ (M is Fe, Co, or FeCo) has been determined in the form of Gibbs free energy, using DFT calculations. In this case, one hydrogen atom is placed over the surface of M@NDC@$MoS_2$ hybrid and the system is optimized. The model sizes of M, NDC, and $MoS_2$ are much smaller than their experimentally observed species, but the essential effect on the electronic structure can be captured from this simple geometry. Generalized gradient approximation (GGA) with the Perdew-Burke-Ernzerhof (PBE) exchange-correlation functional and double ζ Zeta Polarized (DZP) basis set is used for the structural and energy optimization. The significance of this method over hybrid pseudopotentials is reported elsewhere.[37] The linear combination of atomic orbitals (LCAO) method is used for Fe, Co, Mo, S, C, N, and H atoms.[38] A 5×5×2

Monkhorst-Pack k-point sampling was used for structural optimization, and 5x5x5 has been employed for the electronic property simulations.

The overall HER mechanism over the surface of M@NDC@$MoS_2$ catalyst is evaluated with a three-state diagram consisting of an initial $H^+$ state, an intermediate H* state, and $1/2H_2$ as the final product. The H* free energy of ($\Delta G_{H*}$) is already proved to be a key descriptor to characterize the HER activity of the electrocatalyst. Generally, an electrocatalyst with a positive value $\Delta G_{H*}$ leads to low kinetics of hydrogen adsorption. On the other hand, a catalyst with a negative $\Delta G_{H*}$ value is responsible for the low kinetics of the release of a hydrogen molecule. The reasonable value of $\Delta G_{H*}$ should be zero; i.e., the $\Delta G_{H*}$ value for the well-known and highly efficient Pt catalyst is near-zero as $\Delta G_{H*} \approx 0.09$ eV.[39] The $\Delta G_{H*}$ can be calculated with the help of Equation (1).

$$\Delta G_{H*} = \Delta E_{H*} + \Delta E_{ZPE} - T\Delta S_H \quad (1)$$

Here, the $\Delta E$ is total energy change, calculated from the DFT simulations, $\Delta ZPE$ and $\Delta S$ are the changes in zero-point energy and entropy, respectively. T is the room temperature (298.15 K). Recently, it has been reported that the theoretical working potential is independent of the pH. This is due to the free energies of the elementary reactions vary in the same way with pH, thereby, the potential determining step remains constant. So, in order to simplify the simulating results, in this work, the pH=0 is employed. The free energy of hydrogen at standard conditions is assumed as the energy of $1/2H_2$. The entropy of the $H_2$ is taken from the NIST database.[40]

$$\Delta E_{H*} = E_{(H*)} - E_{(*)} - 1/2E_{H2} \quad (2)$$

where $E_{(H*)}$ and $E_{(*)}$ are calculated from the DFT simulations which are of the given surface with and without H adsorption, respectively, and $E(H_2)$ is the DFT energy of a molecular $H_2$ in the gas

phase. Finally, the $\Delta E_{H^*}$ is the binding energy of adsorbed hydrogen. Therefore, Eq. (1) can be rewritten as

$$\Delta G_{H^*} = \Delta E_{H^*} + 0.37eV \quad (3)$$

Equation 3 is the final Equation for calculating the Free Energy of H.

## 3. Results and discussion

### 3.1. Preparation and characterization

The synthesis process (growing) of $MoS_2$ nanosheets on N-doped carbon encapsulated metal particles is shown in **Scheme 1**. The M@NDC catalysts are prepared from the pyrolysis of $K_3[M(CN)_6]_3$ and $M(CH_3CO_2)_2$ precursor and urea. The M@NDC and $Mo_3O_{10}(C_2H_{10}N_2)$ wires (synthesized according to the reported method of Gao et al.) [34] were added to L-cysteine aqueous solution. The reaction mixture was transferred to a Teflon-lined stainless-steel autoclave and kept at 200 °C for 16 h. During the hydrothermal process, L-cysteine dissociated at elevated temperature and produced S species that absorbed on M@NDC. At the same time, $Mo_3O_{10}(C_2H_{10}N_2)$ dissolved into $Mo_3O_{10}$ species and ethylenediamine. The $Mo_3O_{10}$ species react with the absorbed S species and N-doped carbon shell of M@NDC substrates facilitate the growth of $MoS_2$ nanosheets.[27]

The CoFe@NDC, Co@NDC, and Fe@NDC particles were observed by TEM (Fig. S2a-c) respectively, which shows their spherical shape. The size of particles is from nanometers to sub-micrometers with wide distribution. The HETEM image of CoFe@NDC (Fig. S2d) particle shows a core-shell structure. The crystalline core is encapsulated in a few-layer of carbons shell. The lattice spacing of the crystalline core is approximately 0.202 nm, indicating the metallic nature of CoFe alloy, and spacing between layers of the shell is 0.34 nm, which is also consistent with

graphitic carbon (Fig. S2e). Similarly, Co@NDC (Fig. S2f,g) and Fe@NDC (Fig. S2h,i) also show core-shell structure with a well-defined crystalline core, encapsulated in the graphitic shell. The CoFe@NDC nanoparticles (Fig. S3a) are composed of Co, Fe, C, N, and O elements as measured from the X-ray spectrometric (EDX) spectrum. The Co@NDC (Fig. S3b) sample consists of Co, C, N, and O elements, and Fe@NDC (Fig. S3c) product is composed of Fe, C, N, and O elements. The XRD pattern of the $Mo_3O_{10}(C_2H_{10}N_2)$ wires displays major peaks at 10.3, 12.7, 20.6, 23.8, 25.2, 31, 40.6, and 41.8º (Fig. S4a), which are at a similar position as reported by Geo group (Fig. Sa).[34] SEM images of $Mo_3O_{10}(C_2H_{10}N_2)$ product show wires type morphology with high purity and length of up to several micrometers (Fig. S4b,c).

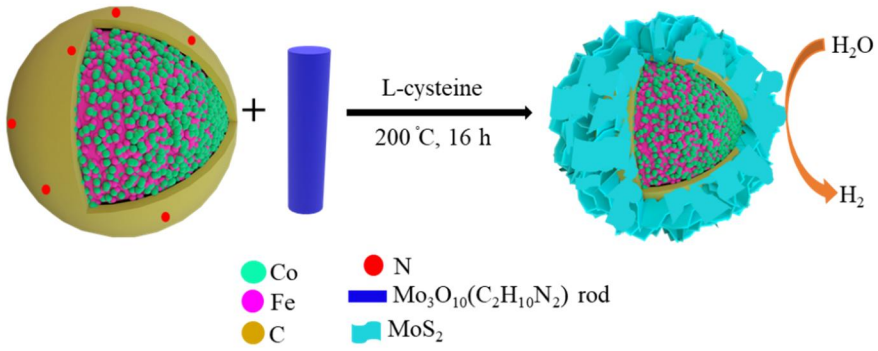


**Scheme 1**. Schematic illustration of the synthesis process of CoFe@NDC@MoS2 hierarchical hybrid sphere.

The SEM images of CoFe@NDC particles after treating with L-cysteine and $Mo_3O_{10}(C_2H_{10}N_2)$ wires are shown in Fig. 1. Comparative SEM analysis of the images led us to predict that the sample is composed of sub-micrometer spherical with hierarchical morphology (Fig. 1a). High magnification SEM images display that the hierarchical structure is composed of nanosheets (Fig. 1b). This suggests that $MoS_2$ nanosheets are vertically grown on CoFe@NDC particles with high

exposed edges. Both hierarchical morphology[41] and exposed edges are useful for enhanced HER catalytic performance.[14] When L-cysteine and $Mo_3O_{10}(C_2H_{10}N_2)$ wires were treated with Co@NDC (Fig. S5a,b) and Fe@NDC (Fig. S5c,d) comparable hierarchical sub-micrometer spherical were observed, indicating the vertical growth of $MoS_2$ on the N-doped carbon shell of M@NDC particles.

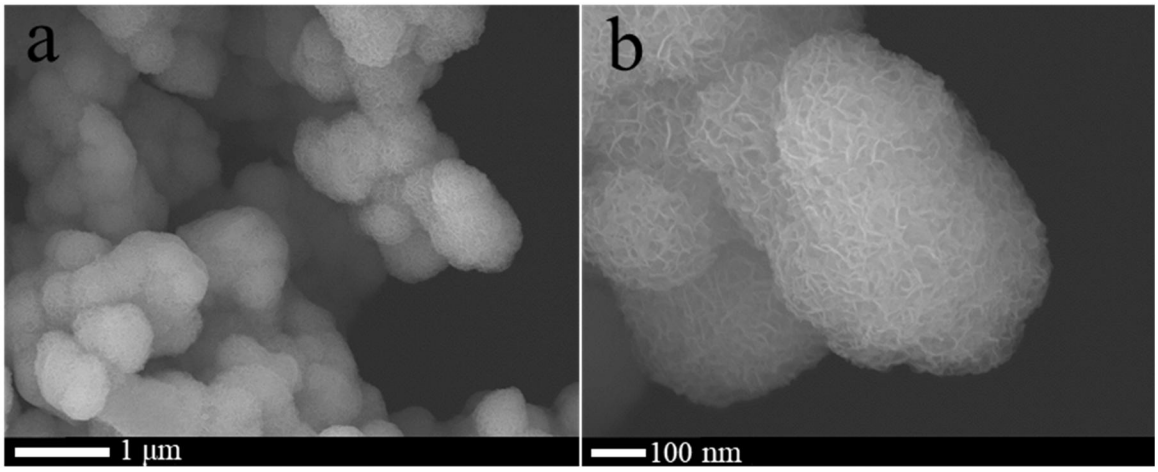


**Fig. 1.** (a,b) SEM images of the CoFe@NDC@$MoS_2$ hybrid.

To further confirm the growth of $MoS_2$ on the M@NDC particles, TEM analysis of the samples was performed. The TEM images of CoFe@NDC@$MoS_2$ display the agglomerated spherical sphere with a hierarchical structure having a size in the range of nanometers to micrometer (Fig. 2a). The dense black center of the hierarchical spherical sphere is surrounded by transparent $MoS_2$ nanosheets as shown in Fig. 2b,c, which suggests few layers of $MoS_2$ nanosheets, grown on the CoFe@NDC particles. When CoFe@NDC@$MoS_2$ hybrid was treated with an acid solution for 30 h, most of the Co and Fe atoms leached out from the core microsphere and hollow hierarchical spheres are obtained as shown in Fig. S6. The Co@NDC@$MoS_2$ (Fig. S7a,b) and Fe@NDC@$MoS_2$ (Fig. S7d,e) also show the agglomerated spherical hierarchical structure with a dense black center and transparent periphery. These similar morphologies of our samples indicate

that the growth sites for $MoS_2$ are located on the N-doped carbon of M@NDC particles. Furthermore, the HETEM image shows the layered structure of $MoS_2$ of CoFe@NDC@$MoS_2$ (Fig. 2d), CoFe@NDC@$MoS_2$. The interlayer spacing of few layers of $MoS_2$ is approximately 0.78, 0.75, and 0.77 nm of CoFe@NDC@$MoS_2$ (Fig. 2e), Co@NDC@$MoS_2$ (Fig. S7c), and Fe@NDC@$MoS_2$ (Fig. S7f), respectively, which is slightly expanded compared to the bulk $MoS_2$ nanosheets.[22,42] We have also observed some defects in the $MoS_2$ nanosheets as shown by arrows in (Fig. 2e). The defects and expanded interlayer spacing can enhance the HER performance of $MoS_2$.[21,22,42] The elemental distribution of CoFe@NDC@$MoS_2$ sample is acquired using EDX attached with TEM. Dark-field TEM images and the elemental mapping images of Mo, S, Co, Fe, C, N, and O, are shown in (Fig. 2f) and (Fig. 2g-m), respectively. The signals of Mo and S elements are homogenous, while that of Co and Fe elements are non-homogenous in elemental mapping images, which suggests the particulate nature of CoFe alloy. On the other hand, the signal for the C element is weaker and weaker in the case of N element. The signals for O elements may arise from the surface oxidation of the composites.

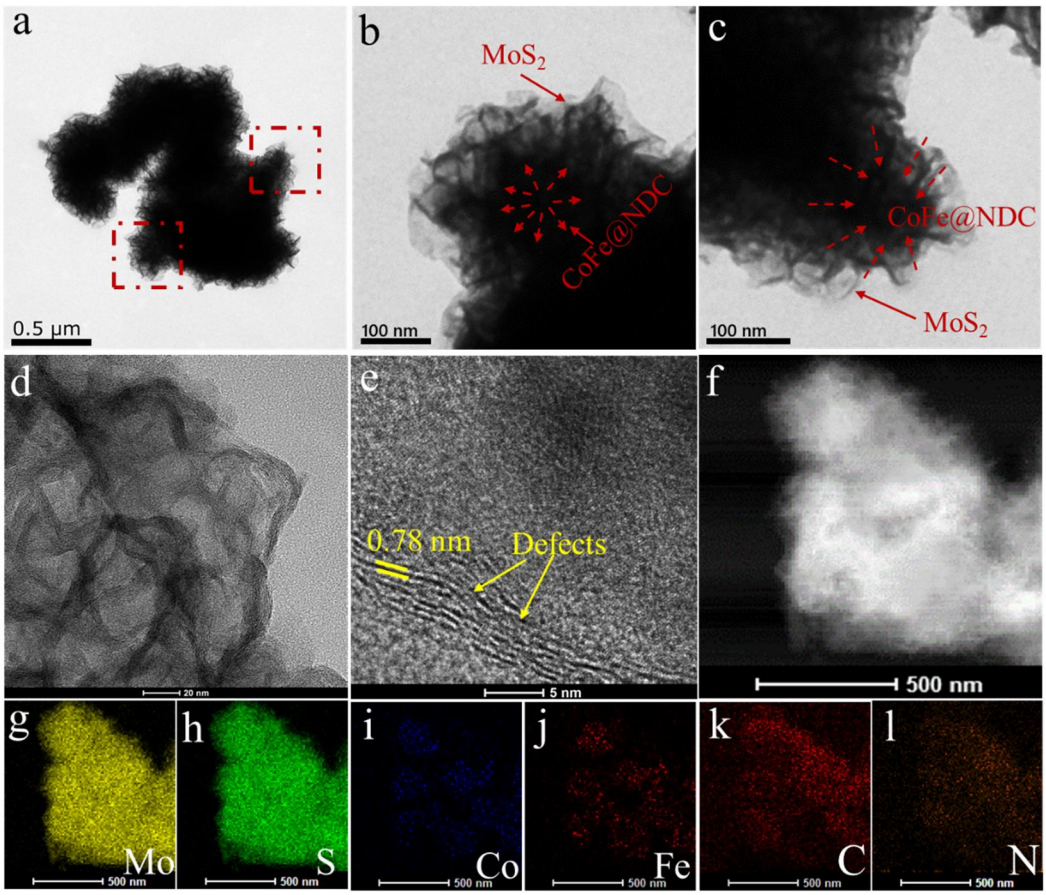


**Fig. 2**. (a-c) TEM and (d,e) HRTEM images of CoFe@NDC@$MoS_2$ hybrid. (f) Dark-field TEM image of CoFe@NDC@$MoS_2$ sample. Elemental mapping images of (g) Mo, (h) S (i) Co (j) Fe (K) C (l) N, and (m) O of CoFe@NDC@$MoS_2$ sample.

XRD patterns of the as-prepared electrocatalyst are shown in Fig. 3a. The diffraction peaks of CoFe@NDC sample show a peak around 44.8° and 65.3° and can be indexed (110) and (200) crystal phase of the cubic CoFe alloy (JCPDS No. 49-1568). The diffraction peaks of Fe@NDC sample around 44.7° and 65° can be assigned to 110 and 200 crystal planes of metallic Fe (JCPDS No. 06-0696), respectively, while peaks around 44.2°, 51.5°, and 75.8° correspond to 111, 200, and 220 crystal planes of metallic Co (JCPDS No. 15-0806) in Co@NDC samples. The diffraction peaks at around 26.2° are associated with characteristic (002) crystal planes of graphitic carbon

(JCPDS No. 04-0850). When $MoS_2$ is grown on the CoFe@NDC, Co@NDC, and Fe@NDC particles, some other diffraction peaks are observed. The obvious diffraction peak at 12.3° can be associated with (002), and very weak peaks in the range of 33-41.2° of hexagonal $MoS_2$ (JCPDS No. 86-2308). The shift of (002) peak of $MoS_2$ nanosheets from 14.5° to 11.2° compared to bulk pristine $MoS_2$, is possibly due to expanded interlayers spacing. Recently, the expanded interlayer spacing of $MoS_2$ nanosheets is reported elsewhere.[22,42] The diffraction peaks at around 26.2° of graphitic carbon broaden after $MoS_2$ growth, indicates the reduction in crystallinity of carbon shell.

The Raman spectra of CoFe@NDC and CoFe@NDC@$MoS_2$ samples are measured which are shown in Fig. 3b. Both samples display the characteristic D-band at 1346 $cm^{-1}$ and G-band at 1584 $cm^{-1}$ for the carbonaceous materials.[43,44] The intensity ratio ($I_D/I_G$) of CoFe@NDC is about 1.2, while the ($I_D/I_G$) of CoFe@NDC@$MoS_2$ is approximately 1.6, this suggests that graphitization of carbon shells is decreased in CoFe@NDC@$MoS_2$ hybrid, The reason behind this reduction is the existence of more defects, caused by $MoS_2$ nanosheets in carbon shells. The relatively weak peaks can be observed in CoFe@NDC@$MoS_2$ hybrid spectrum that is also consistent with in-plane $E^1_{2g}$ (374 $cm^{-1}$) and out-of-plane $A^1_g$ (399 $cm^{-1}$) vibration modes of $MoS_2$.[45,46] The frequency difference ($\Delta k$) is important indicator for layer numbers of $MoS_2$ nanosheets. The $\Delta k$ of $MoS_2$ is 25 $cm^{-1}$ that indicates multilayer $MoS_2$ nanosheets.[45,46]

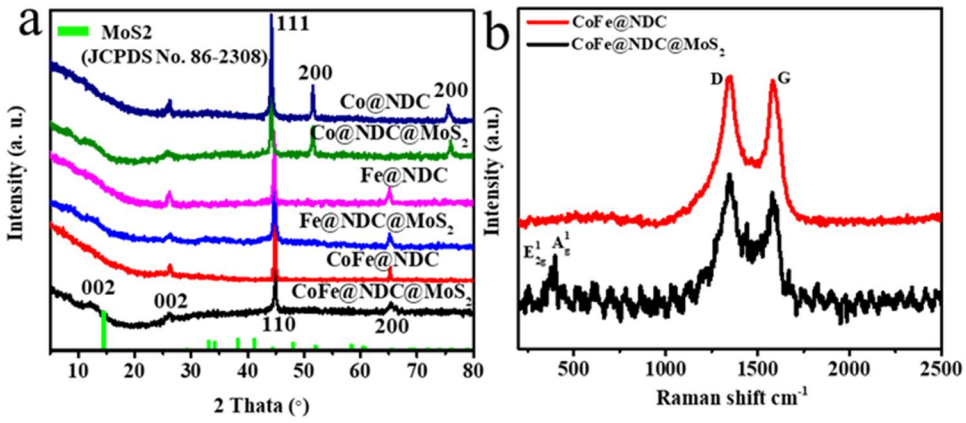


**Fig. 3.** (a) XRD patterns of the as-synthesized samples. (b) Raman spectra of CoFe@NDC particles and CoFe@NDC@$MoS_2$ hybrid.

X-ray photoelectron spectra (XPS) were measured for the elemental composition and valence state of elements of CoFe@NDC@$MoS_2$ composite. The XPS servery spectrum of CoFe@NDC@$MoS_2$ shows well-defined peaks for Mo, S, Co, Fe, C, N, and O elements (Fig. S8). The Mo 3d spectrum can be deconvoluted into four peaks (Fig. 4a). The weak peak with a binding energy of 225.9 eV represents the S 2s.[42,47] The peak of Mo $3d_{5/2}$ at 228.6 eV and Mo $3d_{3/2}$ at 231.8 eV correspond to $Mo^{4+}$ oxidation state in $MoS_2$ compound.[36,41] The peaks centered at 235.6 eV are Mo 3d binding energies of $Mo^{6+}$ oxidation state.[42,47] The XPS spectrum of S 2p displays peaks at 161.6 and 162.8 eV, which are ascribed as S $2p_{3/2}$ and S $2p_{1/2}$ binding energies of $S^{2-}$, respectively (Fig. 4b).[42,47,48] The relatively weak peak at a binding energy of 168.7 eV suggests a low amount of $SO_4^{2-}$ species.[47] The high-resolution XPS spectrum of Co 3p shows peaks at binding energies of 778.2 and 784.3 eV and can be associated to Co $2p_{3/2}$ and Co $2p_{1/2}$ of zero-valent Co, respectively (Fig. 4c).[49.50]

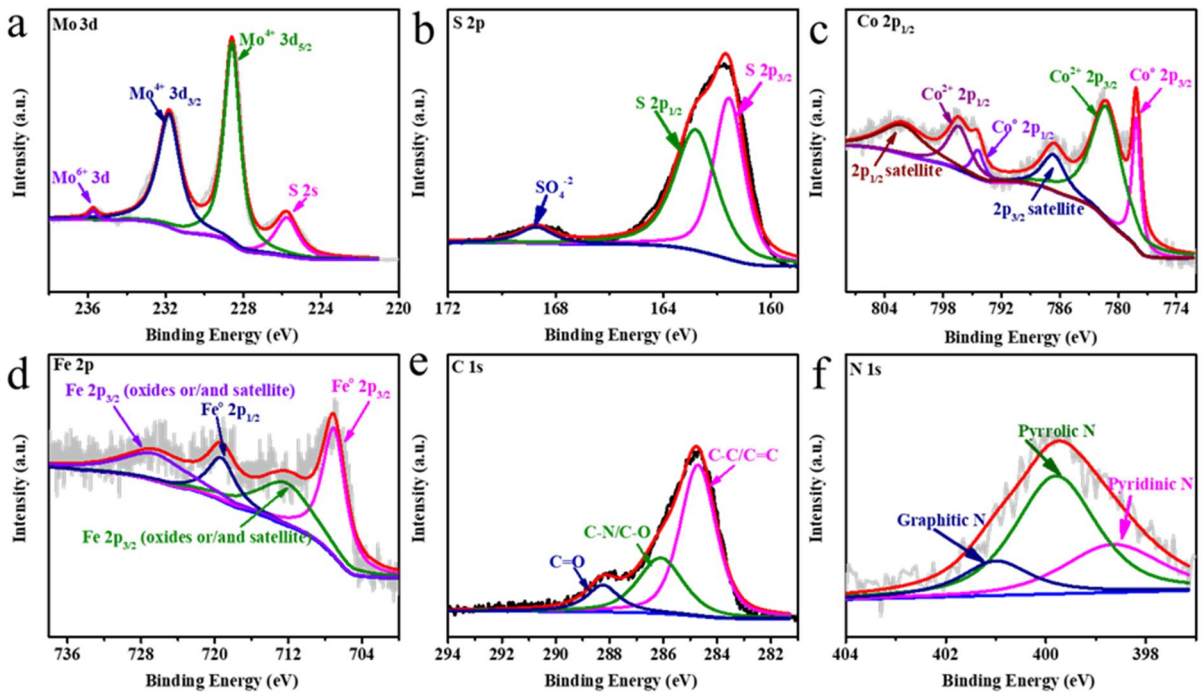


**Fig. 4.** High resolution XPS spectra of (a) Mo 3d, (b) S 2p, (c) Co 2p, (d) Fe 2p, (e) C 1s and (f) N 1s regions of CoFe@NDC@$MoS_2$ hybrid.

The peaks observed at 781.3 and 796.2 eV are allocated to $Co^{2+}$ $2p_{3/2}$ and Co $2p_{1/2}$, respectively.[49,50] The two shakeup satellites are centered at 786.7 and 802.3 eV.[50] These XPS bands of $Co^{2+}$ ions suggest oxidation of the surface atoms of Co. The strong peaks located at binding energies of 707.3 and 720.7 eV can be associated to Fe $2p_{3/2}$ and Fe $2p_{1/2}$ bands which confirm the existence of $Fe^{o}$ in the sample (Fig. 4d).[49,50] The relatively weak peaks at 712.5 and 727.2 eV can be ascribed to the slight oxidation and/or satellites of Fe species.[49,50] The XPS spectra of C 1s region for CoFe@NDC@$MoS_2$ show an intense peak at a binding energy of 284.7 eV and can be associated with C=C/C-C bonding, while relatively weak peaks around 286.1 and 288.2 are possibly related to C-O/C-N and C=O, respectively (Fig. 4e).[51,52] This observation suggests that the degree of graphitization of carbon shells is mostly maintained after

the growth of $MoS_2$. The N1s spectra can be deconvoluted into three types of nitrogen species, pyridinic (398.7 eV), pyrrolic (399.8 eV), and graphitic (401.1 eV) nitrogen (Fig. 4f).[50,53]

### 3.3. Electrocatalytic HER performance of catalysts

Approximately ≈0.28 mg $cm^{-2}$ of the as-synthesized samples were loaded on glassy carbon electrodes in a typical three-electrode system and the electrocatalytic activities for HER performance are evaluated in 0.5 M $H_2SO_4$ aqueous solution, using linear sweep voltammetry (LSV). For comparison, the commercial Pt/C (20 wt%) electrochemical HER performance was also performed under the same conditions. Fig. 5a shows the LSV curves, measured at scan rate 5 mV $s^{-1}$ (*iR* corrected). Among all tested samples, commercial Pt/C shows the best catalytic activity for HER performance with an overpotential of 34 mV at a current density of 10 mA $cm^{-2}$. The CoFe@NDC, Co@NDC, and Fe@NDC demonstrate an overpotential of 307, 367, and 430 mV at a current density of 10 mA $cm^{-2}$, respectively. However, these values are significantly lowered after the growth of $MoS_2$ nanosheets on nanoparticles. The CoFe@NDC@$MoS_2$, Co@NDC@$MOS_2$, and Fe@NDC@$MoS_2$ have improved catalytic performance with an overpotential of 64, 86, and 185 mV at a current density of 10 mA $cm^{-2}$, respectively (Table S1, supplementary data). This result clearly displays that $MoS_2$ nanosheets are mainly responsible for the outstanding HER performance. Specifically, it can be observed that CoFe@NDC@$MoS_2$ hybrids exhibit the best HER performance which is improved almost 4.8 times compared to that of CoFe@NDC. The NDC@$MoS_2$-A and NDC-A samples also show lower performance than those of CoFe@NDC@$MoS_2$ and CoFe@NDC samples, respectively. This further confirmed that the HER activity was mainly due to $MoS_2$ and M@NDC@ $MoS_2$. The CoFe@NDC@$MoS_2$ sample also shows better or comparable HER performance than that of reported $MoS_2$ based

catalysts (Table S2). The excellent HER performance of the obtained sample may be due to the design and fabrication of semiconductor $MoS_2$ on high conductive CoFe@NDC particles.

Analysis of Tafel plots further validates and confirms the estimated HER activities of a catalyst. The Tafel slopes were obtained by fitting the linear portions of LSV carves in the Tafel equation and the corresponding Tafel plot is shown in Fig. 5b. The small values of Tafel slope are considered to be beneficial for the practical application, which reveals the faster reaction kinetics for hydrogen production. The Tafel slope of Pt/C, CoFe@NDC@$MoS_2$, Co@NDC@$MOS_2$, Fe@NDC@$MoS_2$, CoFe@NDC, Co@NDC, Fe@NDC, NDC@$MoS_2$-A, and NDC-A are 30, 45, 57, 67, 94, 146 and 164, 167 and 222 mV $dec^{-1}$, respectively. Principally, the hydrogen evolution mechanism involves three basic reactions for HER in acidic media, including the Volmer reaction ($H_3O^+ + e^- \rightarrow H_{ads} + H_2O$), Heyrovsky reaction ($H_3O^+ + H_{ads} + e^- \rightarrow H_2 + H_2O$), and the Tafel reaction ($H_{ads} + H_{ads} \rightarrow H_2$). The Volmer reaction is the initial discharge step (Tafel slope approximately 120 mV $dec^{-1}$), Heyrovsky reaction is electrochemical desorption step (Tafel slope approximately 40 mV $dec^{-1}$), and Tafel reaction is a recombination step (Tafel slope approximately 40 mV $dec^{-1}$).[21,42] According to Tafel slope values, the rate-limiting step for HER follows Volmer-Heyrovsky or Volmer-Tafel reaction in acidic conditions.[21,42] The Tafel slope value of our sample CoFe@NDC@$MoS_2$ is 45 mV $dec^{-1}$ and mainly follows the Volmer-Heyrovsky reaction pathway for the HER process and a possible rate-determining step is an electrochemical desorption.

The exchange current density ($J_o$) values are determined from the extrapolation method of the Tafel equation (Fig. S9).[42,54] The $J_o$ of Pt/C is 0.98 mA $cm^{-2}$, which is the highest among the tested samples. The $J_o$ of the as-synthesized samples is in the range of 0.75-0.165 mA $cm^{-2}$. The $J_o$ value of CoFe@NDC@$MoS_2$ hybrid (0.750 mA $cm^{-2}$) is higher than all the samples but slightly

lower than that of Pt/C. The $J_o$ value of Co@NDC@$MOS_2$, Fe@NDC@$MoS_2$, CoFe@NDC, Co@NDC, and Fe@NDC is 0.660, 0.223, 0.165, 0.173, and 0.214, respectively. Furthermore, the electrochemical surface area of samples was measured from the electrochemical double-layer capacitances ($C_{dl}$) as shown in Fig. S10. The $C_{dl}$ value of samples are in the order of CoFe@NDC@$MoS_2$, (11.2 mF $cm^{-2}$) > Co@NDC@$MoS_2$, (9.51 mF $cm^{-2}$) > Fe@NDC@$MoS_2$, (1.85 mF $cm^{-2}$) > CoFe@NDC, (0.72 mF $cm^{-2}$) > Co@NDC (0.53 mF $cm^{-2}$) > Fe@NDC (0.21 mF $cm^{-2}$) (Fig. S10g). The higher $C_{dl}$ value of CoFe@NDC@$MoS_2$ suggests it's excellent catalytic activity. The electrochemical impedance spectroscopy (EIS) of the as-prepared samples was also measured which are shown in Fig. 5c. The Nyquist plots of Fig. 5c is fitted, using the equivalent circuit (inset of Fig. 5c). The charge transfer resistance (Rct) values of Fe@NDC, CoFe@NDC, and Co@NDC are 4.92, 11.33, and 20.20 Ω, respectively, while the CoFe@NDC@$MoS_2$, Co@NDC@$MoS_2$, Fe@NDC@$MoS_2$, are 29.40, 45.86, and 195 Ω, respectively. Among the M@NDC@$MoS_2$ hybrids, the CoFe@NDC@$MoS_2$ displays much lower than other samples, suggesting more efficient charge transfer at the electrode/electrolyte interface and contribute to enhancing catalytic performance.

The stability of an electrocatalyst is an important aspect of its long-term hydrogen productions. The stability of the CoFe@NDC@$MoS_2$ catalyst was tested in 0.5 m $H_2SO_4$ solution, measuring CV cycling at a scan rate of 100 mV $s^{-1}$ from 0 to −0.6 *vs*. SEC and chronoamperometric test. The LSV curve of fresh CoFe@NDC@$MoS_2$ sample is used for 2000 CV cycles, as shown in Fig. 5d. It can be seen that LSV curve after 2000 CV cycle shows negligible decay in HER performance as compared to the fresh one. It suggests that our CoFe@NDC@$MoS_2$ catalyst has good stability and can be used for practical application. The SEM images of CoFe@NDC@$MoS_2$ catalyst after 200 CV cycling still show hierarchical spherical morphology of $MoS_2$ nanosheets (Fig. S11),

which further confirm the stability of our catalyst. However, $MoS_2$ nanosheets have rougher morphology compared to the initial one, which may be due to oxidation in the electrochemical process. The TEM displays agglomerated hierarchical structure with a dense black center and transparent periphery (Fig. S12a). The lamellar structure of $MoS_2$ nanosheets is still visible as can be observed from the HETEM image, showing its good stability (Fig. S12b). The main peaks of $MoS_2$ nanosheets, CoFe alloy, and N-doped carbon phases in XRD diffraction are consistant for the fresh and post-HER CoFe@NDC@$MoS_2$ samples (Fig. S13a). The XPS survey spectrum also confirmed the peaks for Co, Fe, Mo, S, C, N, and O elements in composite (Fig. S13b), which suggested the long-term stability and durability of our prepared catalyst. The chronoamperometry curve (inset of Fig. 5d) for CoFe@NDC@$MoS_2$ sample was also measured. The small current density further decline which shows the long-term stability of CoFe@NDC@$MoS_2$ catalyst.

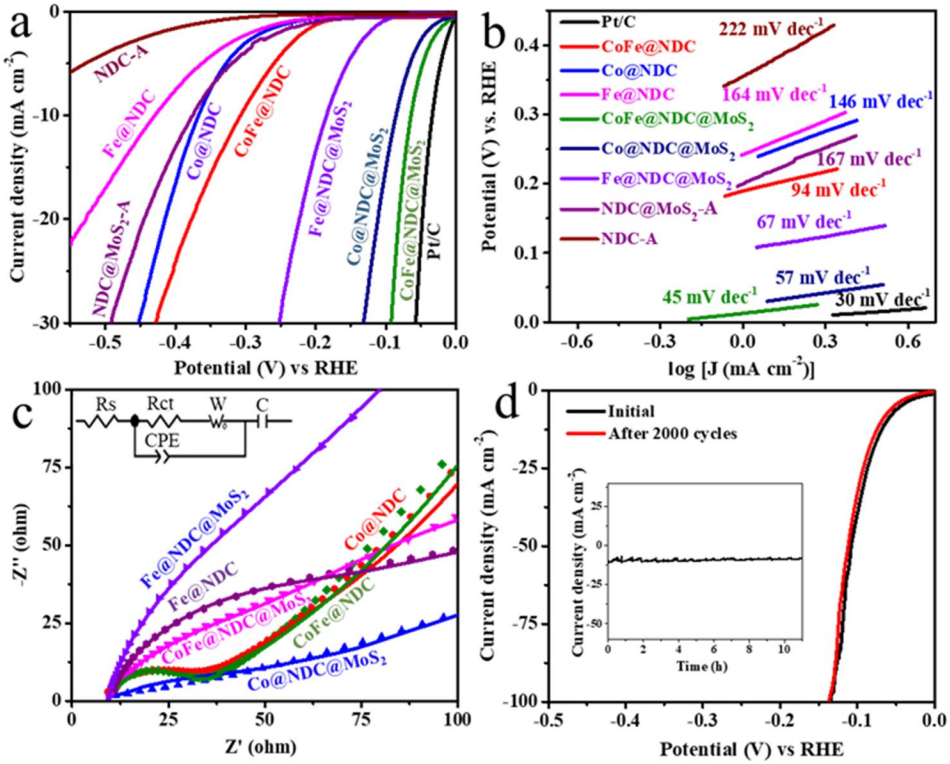

**Fig. 5**. (a) LSV curves of the as-prepared electrocatalyst, acid-treated samples, and commercial 20% Pt/C catalyst. (b) The Tafel plots are derived from LSV carves in "a" of the as-prepared electrocatalyst and commercial 20% Pt/C catalyst. (c) Nyquist plots of the prepared catalyst. Inset shows the equivalent circuit used to fit the experimental data (d) LSV curves of the fresh CoFe@NDC@$MoS_2$ hybrid and after 2000 CV cycles, and chronoamperometric curve (inset of Fig. 5d) to evaluate the stability of catalysts.

### 3.3 First-principles electronic properties

First-principles density functional theory studies are employed to gain insights into M@NDC@$MoS_2$ for its outstanding HER performance. The N-doped carbon encapsulated metal nanoparticles interacted with a single layer of $MoS_2$ nanosheet (see details in computational methodology) and free energy for H adsorption ($\Delta G_{H^*}$) is simulated over the surface of M@NDC@$MoS_2$ (Fig. S1). The calculated $\Delta G_{H^*}$ values of as-prepared samples are plotted in Fig. 6a and Table S3, where the $\Delta G_{H^*}$ value of Fe@NDC, Co@NDC, CoFe@NDC, Fe@NDC@$MoS_2$, Co@NDC@$MoS_2$, and CoFe@NDC@$MoS_2$ are -1.97, -1.93, -1.97, -0.56, 0.10 and -0.08 eV, respectively. An effective electrocatalyst has moderate $\Delta G_{H^*}$ to overcome the reaction barriers in the HER process in both adsorption and desorption steps. Comparative analysis of the data leads us to predict that the $\Delta G_{H^*}$ value of CoFe@NDC@$MoS_2$ is minimum, which is close to the thermodynamic limit value. The theoretical data further confirm and validate the promising performance of CoFe@NDC@$MoS_2$-based electrocatalysts for HER. The high activity is due to the electrostatic interaction of hydrogen with the surface of $MoS_2$ of CoFe@NDC@$MoS_2$ (Fig. S1). On the other hand, the $\Delta G_{H^*}$ value of CoFe@NDC is -1.97 eV, which is due to the strong adsorption energy of H* that consequently hinders the HER process and reduced the catalyst performance. Moreover, the $\Delta G_{H^*}$ value of hydrogen adsorption for Co@NDC, Fe@NDC,

Co@NDC@$MoS_2$, and Fe@NDC@$MoS_2$ also exhibit strong adsorption energy and hinder the hydrogen desorption process. The enhanced HER activity of CoFe@NDC@$MoS_2$ may be due to the interaction of H and S over the surface $MoS_2$ of M@NDC@$MoS_2$, where $H^+$ is adsorbed. The optimal electron transfer from CoFe@NDC nanoparticle to $MoS_2$ nanosheet in CoFe@NDC@$MoS_2$ can be seen in Fig. 6b and Fig. S14, where the electron density on $MoS_2$ surface becomes moderately increased and attracts proton, leading to efficient evolution of hydrogen molecules. The release of hydrogen molecules can be view on the surface of $MoS_2$ in CoFe@NDC@$MoS_2$ catalyst in simulated Video 1 (supporting data). On the other hand, the charge transferring phenomenon in Fe@NDC@$MoS_2$ is high which provides strong attractive forces for protons (Fig. S15). The H* cannot be easily desorbed from the surface of catalyst and consequently lowers the HER performance, while Co@NDC@$MoS_2$ has comparable charge transfer, (Fig. S16) but still higher than that of CoFe@NDC@$MoS_2$.

Furthermore, the enhanced HER activity of CoFe@NDC@$MoS_2$ may be due to an excellent interaction of CoFe@NDC nanoparticles with $MoS_2$ nanosheets. The partial density of states (PDOS) plot of CoFe@NDC@$MoS_2$ is shown in Fig. 6c, where the occupied orbitals of Fe and Co have strong hybridization in the valence band DOS (-10 to 0 eV). The unoccupied anti-bonding orbitals of Fe, Co, Mo, S, N, and C have mutual orbital overlapping in the conduction band DOS (0 to 10 eV). These mutual orbital hybridizations are responsible for the excellent charge transferring and overall stability of CoFe@NDC@$MoS_2$. The PDOS of CoFe@NDC@$MoS_2$ is enhanced compared to CoFe@NDC, especially near the valance band (0 to -10 eV). The Fe and Co atoms interact with NDC shells that exhibit extra features near the Fermi level. Initially, charge transfer occurred between CoFe cluster and NDC, and then CoFe@NDC and $MoS_2$ sheet; which consequently decrease the Fermi level. The work function is simulated from the reciprocal of

Fermi energy, which decreases from 4.48 (CoFe@NDC) to 4.39 eV (CoFe@NDC@$MoS_2$). This effect is further illustrated by the electron difference density (EDD) distribution as shown in Fig. S17.

In addition, this charge transfer generates a local dipole near the interface that decreases the local work function and enhances the chemical reactivity of the functionalized region of the CoFe@NDC@$MoS_2$ exterior. That is why the $\Delta G_{H^*}$ of hydrogen adsorption is minimum over the surface of CoFe@NDC@$MoS_2$ and can further increase the DOS near the Fermi level and reduce the work function of the M@NDC@$MoS_2$ (Fig. S18).

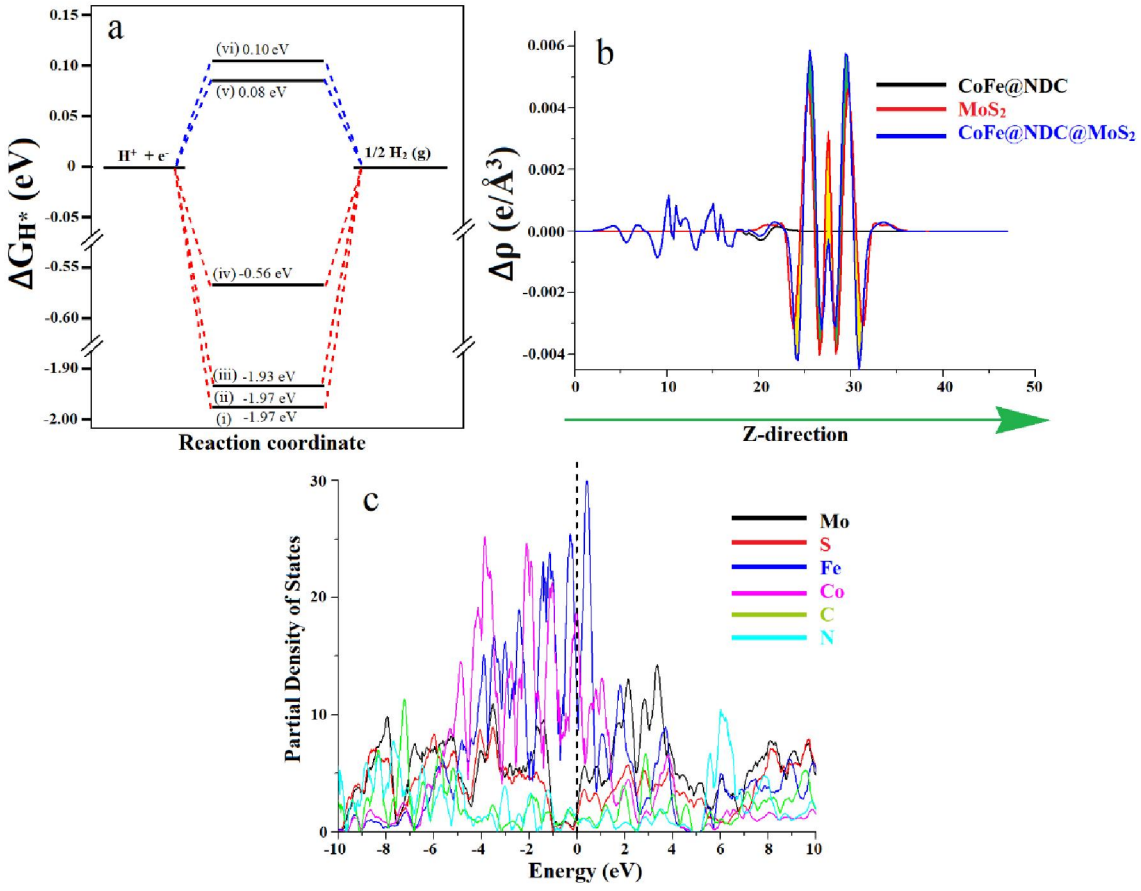


**Fig. 6. (a)** Gibbs free energy ($\Delta G_{H^*}$) of HER process of Fe@NDC (i), CoFe@NDC (ii), Co@NDC (iii), Fe@NDC@$MoS_2$ (iv), CoFe@NDC@$MoS_2$ (v), and CoFe@NDC@$MoS_2$ (vi). (b) average

electron density difference (Δρ) along the Z-direction for CoFe@NDC$MoS_2$ (black line), $MoS_2$ (red line), and CoFe@NDC@$MoS_2$ (blue line). The green and yellow shaded areas indicate electron donation and accumulation, respectively, and (c) Partial density of states plots of CoFe@NDC@$MoS_2$, where the Fermi level is aligned at 0 eV.

## 4 Conclusion

In summary, we have reported an efficient M@NDC@$MoS_2$ hierarchical hybrid spheres HER electrocatalyst, using both theoretical and experimental approaches. Among the prepared samples, CoFe@NDC@$MoS_2$ exhibits excellent HER performance with an overpotential of 64 mV at a current density of 10 mA $cm^{-2}$ and a small Tafel slope of 45 mV $dec^{-1}$. The CoFe@NDC@$MoS_2$ hybrid spheres have good stability and durability in 0.5 M $H_2SO_4$ solution. DFT simulations further validate and confirm the outstanding catalytic activity of CoFe@NDC@$MoS_2$, and suggest that it is due to the optimal electron transfer from $MoS_2$ nanosheets to CoFe@NDC nanoparticles. This electron transferring phenomenon facilitates the $H^+$ interaction and adsorption, leading to a decreased Gibbs free energy ($\Delta G_{H^*} \approx$ 0.08 eV) and local work function on the surface and consequently enhance the HER performance. Besides, it is found that both theory and experiment strongly corroborate each other. Finally, we found that M@NDC@$MoS_2$ hierarchical hybrid spheres is outstanding electrocatalyst for hydrogen production and can be used for various other applications.

## References

1. S. Kampouri, K. C. Stylianou, Dual-functional photocatalysis for simultaneous hydrogen production and oxidation of organic substances, ACS Catal. 9 (2019) 4247-4270.

2. H. Sun, Z. Yan, F. Liu, W. Xu, F. Cheng, J. Chen, Self-supported transition-metal-based electrocatalysts for hydrogen and oxygen evolution, Adv. Mater. 32 (2020) 1806326.
3. Y. Shi, B. Zhang, Recent advances in transition metal phosphide nanomaterials: synthesis and applications in hydrogen evolution reaction, Chem. Soc. Rev. 45 (2016)1529-1541.
4. Q. Ding, B. Song, P. Xu, S. Jin, Efficient electrocatalytic and photoelectrochemical hydrogen generation using $MoS_2$ and related compounds, Chem, 1 (2016) 699-726.
5. Y. Sun, C. Liu, D. C. Grauer, J. Yano, J. R. Long, P. Yang, C. J. Chang, Electrodeposited cobalt-sulfide catalyst for electrochemical and photoelectrochemical hydrogen generation from water, J. Am. Chem. Soc. 135 (2013) 17699-17702.
6. G. Wang, W. Chen, G. Chen, J. Huang, C. Song, D. Chen, Y. Du, C. Li, K. K. Ostrikov, Trimetallic Mo–Ni–Co selenides nanorod electrocatalysts for highly-efficient and ultra-stable hydrogen evolution, Nano Energy 71 (2020)104637.
7. Y. Chen, J. Yu, J. Jia, F. Liu, Y. Zhang, G. Xiong, R. Zhang, R. Yang, D. Sun, H. Liu, W. Zhou, Metallic $Ni_3Mo_3N$ porous microrods with abundant catalytic sites as efficient electrocatalyst for large current density and superstability of hydrogen evolution reaction and water Splitting, Appl. Catal. B-Environ. 272 (2020) 118956.
8. Z. Xing, Q. Liu, A. M. Asiri, X. Sun, High-efficiency electrochemical hydrogen evolution catalyzed by tungsten phosphide submicroparticles, ACS Catal. 5 (2015) 145-149.
9. J. T. Rena, L. Chen, D. D. Yang, Z. Y. Yuan, Molybdenum-based nanoparticles ($Mo_2C$, MoP and $MoS_2$ ) coupled heteroatoms-doped carbon nanosheets for hydrogen evolution reaction, Appl. Catal. B-Environ. 263 (2020) 118352.

10. B. H. R. Suryanto, Y. Wang, R. K. Hocking, W. Adamson, C. Zhao, Overall electrochemical splitting of water at the heterogeneous interface of nickel and iron oxide, Nat. Commun. 10 (2019) 5599.
11. Z. Chen, X. Duan, W. Wei, S. Wang, B. J. Ni, Recent advances in transition metal-based electrocatalysts for alkaline hydrogen evolution, J. Mater. Chem. A 7 (2019) 14971-15005.
12. T. F. Jaramillo, K. P. Jørgensen, J. Bonde, J. H. Nielsen, S. Horch, I. Chorkendorff, Identification of active edge sites for electrochemical $H_2$ evolution from $MoS_2$ nanocatalysts, Science, 317 (2007) 100.
13. C. Jian, W. Hong, Q. Cai, J. Li , W. Liu, Surface electron state engineering enhanced hydrogen evolution of hierarchical molybdenum disulfide in acidic and alkaline media, Appl. Catal. B-Environ. 266 (2020) 118649.
14. S. A. Shah, X. Shen, M. Xie, G. Zhu, Z. Ji, H. Zhou, K. Xu, X. Yue, A. Yuan, J. Zhu, Y. Chen, Nickel@nitrogen-doped carbon@MoS2 nanosheets: An efficient electrocatalyst for hydrogen evolution reaction, Small 15 (2019) 1804545.
15. B. Guo, K. Yu, H. Li, H. Song, Y. Zhang, X. Lei, H. Fu, Y. Tan, Z. Zhu, Hollow structured micro/nano $MoS_2$ spheres for high electrocatalytic activity hydrogen evolution reaction, ACS Appl. Mater. Interfaces 8 (2016) 5517-5525.
16. J. Guo, F. Huob , Y. Chenga, Z. Xiang, PAF-1 as oxygen tank to in-situ synthesize edge-exposed O-$MoS_2$ for highly efficient hydrogen evolution, Catal. Today 347 (2020) 56–62.
17. S. A. Shah, G. Zhu, X. Shen, L. Kong, Z. Ji, K. Xu, H. Zhou, J. Zhu, P. Song, C. Song, A. Yuan, X. Miao, Controllable sandwiching of reduced graphene oxide in hierarchical defect-rich $MoS_2$ ultrathin nanosheets with expanded interlayer spacing for electrocatalytic hydrogen evolution reaction, Adv. Mater. Interfaces 5 (2018) 1801093.

18. X. Dai, K. Du, Z. Li, M. Liu, Y. Ma, H. Sun, X. Zhang, Y. Yang, Co-Doped $MoS_2$ Nanosheets with the Dominant CoMoS phase coated on carbon as an excellent electrocatalyst for hydrogen evolution, ACS Appl. Mater. Interfaces 7 (2015) 27242-27253.
19. X. Zhang, F. Jia, S. Song, Recent advances in structural engineering of molybdenum disulfide for electrocatalytic hydrogen evolution reaction, Chem. Eng. J. 405 (2021) 127013.
20. Z. Chen, X. Liu, P. Xin, H. Wang, Y. Wu, C. Gao, Q. He, Y. Jiang, Z. Hu, S. Huang, Interface engineering of NiS@$MoS_2$ core-shell microspheres as an efficient catalyst for hydrogen evolution reaction in both acidic and alkaline medium, J. Alloys Compd. 853 (2021)157352.
21. J. Xie, H. Zhang, S. Li, R. Wang, X. Sun, M. Zhou, J. Zhou, X.W. Lou, Y. Xie, Defect-rich $MoS_2$ ultrathin nanosheets with additional active edge sites for enhanced electrocatalytic hydrogen evolution, Adv. Mater. 25 (2013) 5807-5813.
22. K. D. Rasamani, F. Alimohammadi, Y. Sun, Interlayer-expanded $MoS_2$, Mater. Today, 20 (2017) 83-91.
23. T. Yang, J. Zhou, T. T. Song, L. Shen, Y. P. Feng, M. Yang, High-throughput identification of exfoliable two-dimensional materials with active basal planes for hydrogen evolution, ACS Energy Lett. 5 (2020) 2313-2321.
24. P. Gnanasekar, D. Periyanagounder, J. Kulandaivel, Vertically aligned $MoS_2$ nanosheets on graphene for highly stable electrocatalytic hydrogen evolution reactions, Nanoscale 11 (2019) 2439-2446.

25. D. J. Li, U. N. Maiti, J. Lim, D. S. Choi, W. J. Lee, Y. Oh, G. Y. Lee, S. O. Kim, Molybdenum sulfide/N-doped CNT forest hybrid catalysts for high-performance hydrogen evolution reaction, Nano Lett. 14 (2014) 1228-1233.
26. M. He, J. Lei, C. Zhou, H. Shi, X. Sun, B. Gao, Growth of vertical $MoS_2$ nanosheets on carbon materials by chemical vapor deposition: influence of substrates, Mater. Res. Express, 6 (2019) 1150c1151.
27. Z. Xiang, Z. Zhang, X. Xu, Q. Zhang, C. Yuan, $MoS_2$ nanosheets array on carbon cloth as a 3D electrode for highly efficient electrochemical hydrogen evolution, Carbon, 98 (2016) 84-89.
28. S. Wang, B. Y. Guan, L. Yu, X. W. Lou, Rational Design of Three-layered $TiO_2$@Carbon@$MoS_2$ hierarchical nanotubes for enhanced lithium storage, Adv. Mater. 29 (2017) 1702724.
29. X. Zhang, L. Huang, P. Zeng, L. Wu, Q. Shen, Z. Gao, Y. Chen, Hierarchical $MoS_2$ anchored on core-shell Si@C with increased active-sites and charge transfer for superior cycling and rate capability in lithium-ion batteries, Chem. Eng. J. 357, (2019) 625-632.
30. D.W. Kim, A.R. Park, T.S. Oh, N.E. Lee, P.J. Yoo, J.B. Yoo, Porous $MoS_2$@C heteroshell with a Si yolk structure with improved lithium transport properties and superior cycle stability, J. Mater. Chem. A 5, (2017) 14906-14913.
31. J. Deng, P. Ren, D. Deng, X. Bao, Enhanced electron penetration through an ultrathin graphene layer for highly efficient catalysis of the hydrogen evolution reaction, Angew. Chem., Int. Ed. 54 (2015) 2100-2104.
32. M. Tavakkoli, T. Kallio, O. Reynaud, A. G. Nasibulin, C. Johans, J. Sainio, H. Jiang, E. I. Kauppinen, K. Laasonen, Single-shell carbon-encapsulated iron nanoparticles: synthesis

and high electrocatalytic activity for hydrogen evolution reaction, Angew. Chem., Int. Ed. 54, (2015) 4535-4538.

33. Y. Xu, W. Tu, B. Zhang, S. Yin, Y. Huang, M. Kraft, R. Xu, Nickel nanoparticles encapsulated in few-Layer nitrogen-doped graphene derived from metal–organic frameworks as efficient bifunctional electrocatalysts for overall water splitting, Adv. Mater. 29 (2017) 1605957.
34. Q. Gao, S. Wang, H. Fang, J. Weng, Y. Zhang, J. Mao, Y. Tang, One-dimensional growth of $MoO_x$-based organic–inorganic hybrid nanowires with tunable photochromic properties, J. Mater. Chem. 22 (2012) 4709-4715.
35. Atomistix Tool Kit version 2019.12, Quantum Wise A/S (www.quantumwise.com).
36. VirtualNanoLab version 2019.12, QuantumWise A/S (www.quantumwise.com).
37. A. H. Larsen, M. Vanin, J. J. Mortensen, K. S. Thygesen, K. W. Jacobsen, Localized atomic basis set in the projector augmented wave method, Phys. Rev. B, 80 (2009) 195112.
38. G. Kresse, D. Joubert, From ultrasoft pseudopotentials to the projector augmented-wave method, Phys. Rev. B, 59 (1999) 1758.
39. J. K. Nørskov, T. Bligaard, A. Logadottir, J. Kitchin, J. G. Chen, S. Pandelov, U. Stimming, Trends in the exchange current for hydrogen evolution, J. Electrochem. Soc. 152 (2005) J23.
40. M. W. Chase, NIST-JANAF thermochemical tables for oxygen fluorides, J. Phys. Chem. Ref. Data, 25 (1996) 551-603.
41. J. Zhang, S. Liu, H. Liang, R. Dong, X. Feng, Hierarchical transition-metal dichalcogenide nanosheets for enhanced electrocatalytic hydrogen evolution, Adv. Mater. 27 (2015) 7426-7431.

42. Y. J. Tang, Y. Wang, X. L. Wang, S. L. Li, W. Huang, L. Z. Dong, C. H. Liu, Y. F. Li, Y. Q. Lan, Molybdenum disulfide/nitrogen-doped reduced graphene oxide nanocomposite with enlarged interlayer spacing for electrocatalytic hydrogen evolution, Adv. Energy Mater. 6 (2016) 1600116.
43. A. C. Ferrari, D. M. Basko, Raman spectroscopy as a versatile tool for studying the properties of graphene, Nat. Nanotechnol. 8 (2013) 235-246.
44. S. A. Shah, Z. Ji, X. Shen, X. Yue, G. Zhu, K. Xu, A. Yuan, N. Ullah, J. Zhu, P. Song, X. Li, Thermal synthesis of FeNi@nitrogen-doped graphene dispersed on nitrogen-Doped carbon matrix as an excellent electrocatalyst for oxygen evolution reaction, ACS Appl. Mater. Interfaces 2 (2019) 4075-4083.
45. Y. Yu, C. Li, Y. Liu, L. Su, Y. Zhang, L. Cao, Controlled scalable synthesis of uniform, high-quality monolayer and few-layer $MoS_2$ films, Sci. Rep. 3 (2013) 1866.
46. Z. Deng, H. Jiang, Y. Hu, Y. Liu, L. Zhang, H. Liu, C. Li, 3D Ordered macroporous $MoS_2$@C nanostructure for flexible Li-ion batteries, Adv. Mater. 29 (2017) 1603020.
47. Y. H. Chang, C. T. Lin, T. Y. Chen, C. L. Hsu, Y. H. Lee, W. Zhang, K. H. Wei, L. J. Li, Highly efficient electrocatalytic hydrogen production by $MoS_x$ grown on graphene-protected 3D Ni foams, Adv. Mater. 25 (2013) 756-760.
48. V. O. Koroteev, L. G. Bulusheva, I. P. Asanov, E. V. Shlyakhova, D. V. Vyalikh, A.V. Okotrub, Charge transfer in the $MoS_2$/Carbon nanotube composite, J. Phys. Chem. C. 115 (2011) 21199-21204.
49. Y. Yang, Z. Lin, S. Gao, J. Su, Z. Lun, G. Xia, J. Chen, R. Zhang, Q. Chen, Tuning electronic structures of nonprecious ternary alloys encapsulated in graphene layers for optimizing overall water splitting activity, ACS Catal. 7, (2017) 469-479.

50. B. K. Barman, K. K. Nanda, CoFe nanoalloys encapsulated in N-doped graphene layers as a Pt-Free multifunctional robust catalyst: elucidating the role of Co-alloying and N-doping, ACS Sustain, Chem, Eng. 6 (2018) 12736-12745.
51. S. A. Shah, G. Zhu, A. Yuan, N. Ullah, X. Shen, H. Khan, K. Xu, X. Wang, X. Yan, Loading of individual Se-doped $Fe_2O_3$-decorated Ni/NiO particles on carbon cloth: facile synthesis and efficient electrocatalysis for the oxygen evolution reaction, Dalton Trans. 49 (2020) 15682-15692.
52. K. Li, X. Jian, S. Li, W. Wang, Y. Lei, P. Zhang, J. Liu, C. Zhou, L. Chen, In situ growth of urchin-like cobalt–chromium phosphide on 3D graphene foam for efficient overall water splitting, Inorg. Chem. Front. 7 (2020) 4913-4923.
53. C. Song, S. Wu, X. Shen, X. Miao, Z. Ji, A. Yuan, K. Xu, M. Liu, X. Xie, L. Kong, G. Zhu, S. Ali Shah, Metal-organic framework derived Fe/$Fe_3C$@N-doped-carbon porous hierarchical polyhedrons as bifunctional electrocatalysts for hydrogen evolution and oxygen-reduction reactions, J. Colloid Interface Sci. 524 (2018) 93-101.
54. Y. J. Tang, M. R. Gao, C. H. Liu, S. L. Li, H. L. Jiang, Y. Q. Lan, M. Han, S. H. Yu, Porous molybdenum-based hybrid catalysts for highly efficient hydrogen evolution, Angew. Chem., Int. Ed. 54 (2015) 12928-12932